

HYDRODYNAMICAL SIMULATIONS OF COLLIDING JETS: MODELING 3C 75

S. M. MOLNAR¹, H.-Y. SCHIVE², M. BIRKINSHAW³, T. CHIU^{4,5}, G. MUSOKE³, AND A. J. YOUNG³

Draft version December 8, 2016

ABSTRACT

Radio observations suggest that 3C 75, located in the dumbbell shaped galaxy NGC 1128 at the center of Abell 400, hosts two colliding jets. Motivated by this source, we perform three-dimensional hydrodynamical simulations using a modified version of the GPU-accelerated Adaptive-Mesh-Refinement hydrodynamical parallel code (*GAMER*) to study colliding extragalactic jets. We find that colliding jets can be cast into two categories: 1) bouncing jets, in which case the jets bounce off each other keeping their identities, and 2) merging jets, when only one jet emerges from the collision. Under some conditions the interaction causes the jets to break up into oscillating filaments of opposite helicity, with consequences for their downstream stability. When one jet is significantly faster than the other and the impact parameter is small, the jets merge; the faster jet takes over the slower one. In the case of merging jets, the oscillations of the filaments, in projection, may show a feature which resembles a double helix, similar to the radio image of 3C 75. Thus we interpret the morphology of 3C 75 as a consequence of the collision of two jets with distinctly different speeds at a small impact parameter, with the faster jet breaking up into two oscillating filaments.

Subject headings: galaxies: clusters: general – galaxies: clusters: individual (Abell 400) – galaxies: clusters: intracluster medium – methods: numerical – extragalactic jets

1. INTRODUCTION

Extragalactic jets are thought to play an important role in providing a heating mechanism in the center of cool core (CC) clusters of galaxies. CC clusters exhibit a falling temperature and increasing gas density towards their center (for a review see Fabian 1994). The high temperature (few million Kelvin) intracluster gas (ICG) cools mainly via thermal bremsstrahlung and line emission, the cooling time being proportional to the inverse of the gas density. The cooling times in the dense core of some CC clusters are much shorter than the Hubble time.

As a consequence of the short cooling times, we expect a large amount of cool gas and high star formation rate in these clusters. However, X-ray observations made by *Chandra* and *XMM-Newton* (e.g., Peterson et al. 2003; Tamura et al. 2003; Peterson & Fabian 2006) did not find a large amount of cool gas in CC galaxy clusters, and the observed star formation rate is much lower than predicted (e.g., Edge 2001; Salomé & Combes 2003; McDonald, Veilleux & Mushotzky 2011; O’Dea et al. 2008). Non-gravitational energy input into CC clusters seems to be necessary to solve this, the so called “cooling flow” problem. This energy input is most likely self-regulated, since it should provide sufficient heat to quench the cooling, but at the same time it should not be so strong as to overheat and destroy the cool core. The most likely sources providing the sufficient heating to prevent the

intracluster gas from runaway cooling are active galactic nuclei (AGNs) located at the center of CC clusters (McNamara & Nulsen 2007), but the exact physical mechanism which distributes that heat is still not known.

Recent high resolution observations indicate that active galactic nuclei (AGNs) at the center of CC clusters of galaxies generate hot bubbles, jets, shocks, and turbulence in the ICG (see Fabian 2012 for a review). Jets have been suggested as the main source of energy input from AGNs into the ICG. Numerical simulations have demonstrated that AGN feedback based on momentum-driven jets can prevent the cooling catastrophe (e.g., Gaspari et al. 2011; Martizzi et al. 2012). Simulations assuming that the AGNs are powered by the accretion of cold gas produced stable thermal equilibrium and multiphase filamentary structures similar to those observed in nearby CC clusters (e.g., Gaspari et al. 2012; Li & Bryan 2014a; Gaspari et al. 2013). However, the cold gas forms an unrealistically massive stable disk in simulations, suggesting that other physical processes are necessary to explain the observations (Li & Bryan 2014b).

It was proposed and demonstrated by Falceta-Gonçalves et al. (2010) that the combined effect of star formation and AGN feedback to prevent the cooling catastrophe. More recently, Li et al. (2015) demonstrated that momentum-driven AGN feedback and star formation can prevent the cooling catastrophe producing self-regulated cycles of accretion by the central supermassive black hole, which heats the gas, followed by gas cooling until the next cycle. This model is mainly consistent with most observations (but, e.g., occasionally, it does produce higher star formation rate and cooling rate than observations imply). However, more work is needed to improve the model parameters and include more physics (e.g., transport processes and magnetic fields, which may provide additional pressure support, and likely suppress star formation and lower the star formation rate; van

¹ Institute of Astronomy and Astrophysics, Academia Sinica, P. O. Box 23-141, Taipei 10617, Taiwan

² National Center for Supercomputing Applications, Urbana, IL, 61801, USA

³ HH Wills Physics Laboratory, University of Bristol, Tyndall Avenue, Bristol BS8 1TL, UK

⁴ Department of Physics, National Taiwan University, Taipei 106, Taiwan

⁵ Center for Theoretical Sciences, National Taiwan University, Taipei 106, Taiwan

Loo et al. 2015). Magnetic fields are essential in launching and collimating the jets, but perhaps less important for jets propagating on extragalactic scales (e.g., Pudritz et al. 2012). Most recent magneto-hydrodynamical simulations including AGN feedback, cooling, and anisotropic conduction due to the jet magnetic field show that the main sources of heating are still AGNs, however, conduction may contribute to heating significantly in the most massive clusters only if the maximum Spitzer conductivity is adopted along magnetic field lines (Yang & Reynolds 2016).

The collisions of jets are extremely energetic events, thus they offer a unique opportunity to study astrophysical plasma under extreme conditions and infer the physical properties of jets based on the comparison of hydrodynamical (and magneto-hydrodynamical) simulations with observations. Jet collisions are also rare, but radio observations of the double twin-jet system, 3C 75, located in NGC 1128 at the center of the nearby galaxy cluster Abell 400, suggest that there are two colliding jets (e.g., Hudson et al. 2006). In Figure 1 we show superimposed radio and optical images of the centre of 3C 75. The western jet from the northern AGN appears to collide with, and merge into, the northern jet from the southern AGN which does not seem to change its course significantly.

Motivated by 3C 75, we study the interaction between two bipolar jets by performing hydrodynamical simulations using a modified version of the GPU-accelerated Adaptive-Mesh-Refinement (AMR) hydrodynamical parallel code (*GAMER*) developed at the Institute of Astrophysics of National Taiwan University (Schive et al. 2010).

We present our results in the following sections. After this introduction we describe our numerical scheme (Section 2). In Section 3 we present the results of our hydrodynamical simulations of colliding jets and provide a possible physical explanation for the twisted morphology of the jets systems of 3C 75. Section 4 contains our conclusions.

2. HYDRODYNAMICAL SIMULATIONS OF COLLIDING JETS

The formation of jets around AGNs and their propagation out of the host galaxy into the intracluster environment involves complicated non-linear physical processes including non-gravitational physics on a large dynamical range in the space and time domain. Presently it is not feasible to carry out numerical simulations to cover all relevant physical process from the formation and propagation of extragalactic jets from a scale of one pc to tens of kpc. We expect that the jets are launched at relativistic speeds ($\sim 0.98c$) from their AGNs, but they are significantly decelerated by the time they reach the edge of their host galaxies ($\sim 0.4c$), and further decelerate in the intergalactic medium (e.g., Laing & Bridle 2014). In our study we focus on simulating collisions between jets from FR I sources. FR I jets are expected to decelerate significantly, to $v_{jet} \lesssim 0.1c$ on kpc scales (e.g., Feretti et al. 1999; Laing et al. 1999). We modeled the jets as bipolar outflows of high temperature, light fluid launched from cylindrical nozzles at the center of our simulation box with velocities that are expected for these jets when they propagate to extragalactic distances. Since we

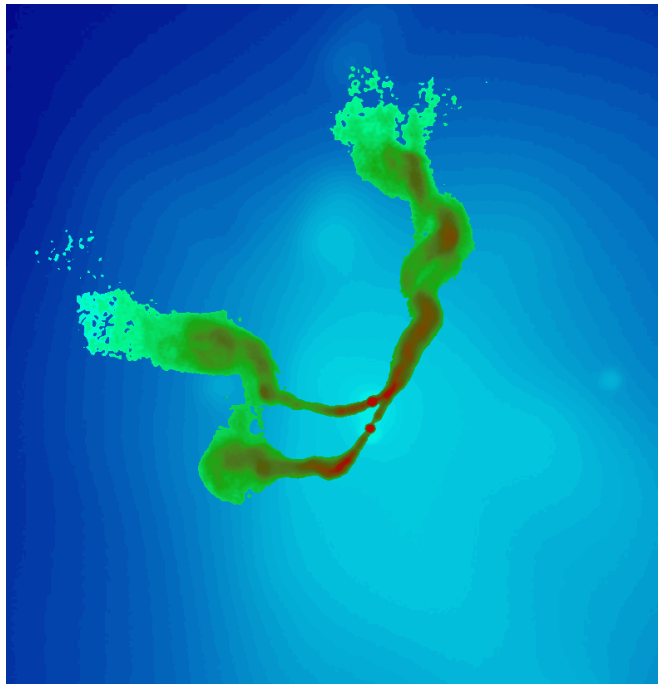


FIG. 1.— Superimposed radio (Very Large Array 8.4 GHz; green and red) and X-ray *Chandra* in 0.7–7.0 keV; blue) image of 3C 75 in NGC 1128 at the center of Abell 400 (after Hudson et al. 2006). The distance between the two AGNs is about 7 kpc in projection.

deal with non-relativistic jet velocities, we may adopt the equations of ideal non-relativistic hydrodynamics.

In our first study of jet collisions, we assumed an initially homogeneous isothermal ambient gas and a continuous inflow of gas with constant injection velocity, and fixed density and temperature for each of the two stationary jets.

We used a modified version of the GPU-accelerated Adaptive-Mesh-Refinement (AMR) hydrodynamical parallel code (*GAMER*) developed at the National Taiwan University (Schive et al. 2010; Schive 2012) to carry out our simulations of colliding jets. *GAMER* adopts a novel approach in improving the performance of astrophysical numerical simulations. It uses GPUs for solving the partial differential equations, for example, hydrodynamics, self-gravity, and magnetohydrodynamics (Zhang et al., in preparation), and uses CPUs for manipulating the AMR data structure. The parallel performance has been highly optimized by implementing (1) hybrid MPI/OpenMP/GPU parallelization, (2) concurrent execution between multiple CPUs and GPUs, (3) asynchronous data transfer between CPUs and GPUs, and (4) Hilbert space-filling curve for load balancing. The code supports a variety of hydrodynamic schemes. In this work we adopt the corner-transport-upwind method (Colella 1990), Roe’s Riemann solver (Roe 1981), and the piecewise parabolic data reconstruction (Colella & Woodward 1984). The overall performance using these schemes is measured to be $\sim 7 \times 10^7$ cell updates per second on a single NVIDIA K40 GPU, which is found to be two orders of magnitude faster than a single CPU core and one order of magnitude faster than a ten-core CPU using an Intel Xeon E5-2670 v2 CPU at 2.50 GHz. The accuracy of *GAMER* has

been carefully verified (Schive et al. 2010; Schive 2012). We also tested *GAMER* by comparing results of bipolar single jet simulations carried out with *GAMER* and the publicly available and extensively tested Eulerian parallel code *FLASH* developed at the University of Chicago (Fryxell et al. 2000).

GAMER solves the Euler equations in conservation form. In this case, in Cartesian coordinates, (x_1, x_2, x_3) , the mass, momentum and energy conservation equations may be expressed as:

$$\frac{\partial \rho}{\partial t} + \frac{\partial}{\partial x_j}(\rho v_j) = 0 \quad (1)$$

$$\frac{\partial(\rho v_i)}{\partial t} + \frac{\partial}{\partial x_j}(\rho v_i v_j + p \delta_{ij}) = 0 \quad (2)$$

$$\frac{\partial e}{\partial t} + \frac{\partial}{\partial x_j}[(e + p)v_j] = 0, \quad (3)$$

where ρ , p , and e are the mass density, the thermal pressure, and the total energy density of the gas, $e = (1/2)\rho v^2 + \epsilon$, where ϵ is the internal energy density, v_i and v_j are the components of the flow velocity vector, \mathbf{v} , and the spatial indices, i , and j take a value of 1, 2, or 3. All dependent physical variables are evaluated at position $\mathbf{r} = (x_1, x_2, x_3)$ and time t (we suppressed the independent variables for clarity). This set of equations is closed by using the equation of state for ideal gas:

$$p = (\gamma - 1)\epsilon, \quad (4)$$

where γ is the ratio of specific heats. For monoatomic classical and ultra-relativistic ideal gases, the adiabatic index changes between 5/3 and 4/3. We adopt $\gamma \leq 5/3$ as a good approximation, since we assume that the jet temperatures are in the non-relativistic regime ($T_{jet} \ll 10^5$ keV; e.g., Mignone & McKinney 2007).

2.1. Initial Conditions for Colliding Jets

We performed simulations of two bipolar jets with different injection velocities, cross sections, densities, and temperatures for the jets and the ambient gas. In this paper we present simulations relevant to our qualitative analysis of colliding extragalactic jets.

With future applications in mind, we chose the physical parameters of our jet system to match those derived for 3C 75 based on radio and X-ray observations (Hudson et al. 2006). We fixed the initial density and temperature for the ambient gas at values suggested by the observations of 3C 75, and adopted a gas density and temperature of $\rho_{amb} = 5 \times 10^{-29}$ g cm $^{-3}$ and $T_{amb} = 0.15$ keV. We simulated both sides of the two bipolar jets to model 3C 75 in a simulation box size of 20 kpc \times 100 kpc \times 20 kpc, $[(x_1, x_2, x_3) = [x, y, z] = [\pm 10, \pm 50, \pm 10]$ kpc) choosing the y axis as the direction of the main jet propagation. We used outflow boundary conditions which are suitable for colliding jets.

The jets were continuously ejected from two nozzles aligned with the (x, y) plane centered at $y = 0$ with a fixed distance of 8 kpc between them (in x) and an offset in the z direction: $\mathbf{r}_{1,2} = (\pm 4 \text{ kpc}, 0, \pm z_0)$, where z_0 defines the impact parameter, $P = 2z_0$, the offset between the two centers of the nozzles. We illustrate our computational setup in Figure 2, where we show the total energy density of one of our models (model P060V18;

see Table 1) projected to the (x, y) plane. The z axis is pointing out of the (x, y) plane with (x, y, z) forming a right handed Cartesian coordinate system. Hereafter we will express the impact parameter in units of the jet diameter, $P = 2z_0/2r_{jet}$, thus $P = 0$ means a head-on collision. When the two jets do not encounter, $P \geq 1$. With a viewing angle of 20° , this gives a projected distance of 7.5 kpc for the jet sources (AGNs), which is in agreement with that of 3C 75 (Hudson et al. 2006).

We adopt a setup for initial conditions suggested by the observed morphology of 3C 75. All intrinsic parameters describing the injection of the two jets were the same: the jet radius: $r_{jet} = 0.35$ kpc, the length of the nozzle: 0.7 kpc (the radius and the height of the cylindrical nozzles). The directions of the jet injection velocity vectors were fixed in the (x, y) plane with directions: $\mathbf{n}_{1,2} = (\pm 1, 3, 0)/\sqrt{10}$. The velocity field within each nozzle generating the bipolar jets was changed smoothly from $-v_i$ to $+v_i$ ($i = 1, 2$) towards the negative and the positive y axis to avoid a large unphysical jump between velocities within adjacent simulation cells, which could cause numerical problems. We adopted $\rho_{jet} = 10^{-30}$ g cm $^{-3}$ and $T_{jet} = 12.2$ keV for the gas of the jets, so the jet is roughly in pressure equilibrium with the ambient medium.

We ran jet collision simulations with a set of different impact parameters changing z_0 , and, fixing one jet velocity at $v_1 = 18000$ km s $^{-1}$, with different velocities of the second jet from $v_2 = 10000$ km s $^{-1}$ to $v_2 = 18000$ km s $^{-1}$ (internal jet Mach numbers, $M_{jet} = v_2/c_{s2}$, where c_{s2} is the sound speed inside the second jet, $4.4 \leq M_{jet} \leq 7.9$; see the input parameters and the IDs for our different models in Table 1). In order to study the jet interactions considering an extensive range of values of the impact parameter, we also ran an additional simulation with a large impact parameter ($P = 1.3$; model P130V18). We ran most of our hydrodynamical simulations for 50 Myr. In those cases when we adopted slow injection velocities for the second jet ($v_2 = 10000, 12000$ km s $^{-1}$), we ran the simulations for 70 Myr in order to make sure that the slower jet propagates well away from the collision region.

3. RESULTS

3.1. Bouncing and Merging of Extragalactic Jets

We show the results of our colliding jet simulations in Figures 3 and 4 as projections of the total energy density on the (x, y) plane, the plane of jet propagation, and the (x, z) plane, showing the interacting jet offsets ($\pm z_0$). The columns of these figures show simulations with different impact parameters, $P = 0, 0.15, 0.3, 0.45, 0.6$, and 0.8 times the diameter of the jet (left to right). The rows show the simulations at different velocities for the second jet expressed as the jet Mach number, $M_{jet} = 7.9, 7.0, 6.1, 5.3$, and 4.4 (top to bottom; see Section 2.1 and Table 1 for details).

The collision regions can be seen clearly in these figures as an enhancement in the projected energy marked by red. In each panel in Figure 3, the two jets are moving from left to right nearly parallel to the horizontal axis (simulation y axis). In Figure 4 the first jet with fixed Mach number ($M_{jet} = 7.9$) is moving left to right, the second jet, with different velocities, is moving in the

opposite direction.

In the first column in Figures 3 and 4 we show jet collisions with zero impact parameter ($P = 0$). In all these cases only one jet seems to emerge after the collision (see Figure 3). However, because of symmetry, after the collision these jets are somewhat spread out in the out-of-collision-plane direction (z ; see Figure 4).

In most of those cases where we adopted a finite impact parameter ($P > 0$), two jets can be seen after the collision. As a consequence of the large velocities, the jets bounce off each other and survive as individuals (see Figure 3). In Figure 3 we can see that after the collision, the jets show increasing instabilities as the impact parameter is decreased, and in some cases, as a result of growing instabilities, the jets break up into oscillating filaments.

After the collision the two jets still propagate in roughly the same plane (see Figure 4), but the plane is rotated relative to the horizontal direction by an angle which is larger for smaller impact parameters and larger velocity differences between the two jets.

In those cases when the second jet is much slower than the first, the two jets may merge, and the bending angle after collision of the slower jet is larger for higher velocity differences between the two jets (see Figure 3).

Based on our results, we can classify colliding jets into two categories: (1) bouncing and (2) merging jets. We illustrate the difference between these two categories in the first and second columns in Figure 5. In this figure we display the total energy density, scaled entropy per particle ($K \propto T/\rho^{2/3}$), enstrophy, $\Omega = (1/2)\omega^2$ (see Section 3.3), and helicity, $\mathbf{v} \cdot \boldsymbol{\omega}$, where $\boldsymbol{\omega}$ is the vorticity, $\boldsymbol{\omega} = \nabla \times \mathbf{v}$, projected to the (x, y) plane (from top to bottom, first two columns). The first column illustrates bouncing of two fast jets with $v_1 = v_2 = 18000 \text{ km s}^{-1}$, and a large impact parameter, $P = 0.8$ (model P080V18); the second column shows projections of a merging jet simulation with a small impact parameter, $P = 0.3$, and large velocity difference: $v_1 = 18000 \text{ km s}^{-1}$ vs. $v_2 = 10000 \text{ km s}^{-1}$ (model P030V10). The jets propagate from left to right. The point of collision is in the middle of the left hand side of the energy panels marked with red (see top left panel for each simulation). It can be seen clearly from Figure 5 that, after the collision, the bouncing jets (1st column) keep their identities and travel relatively unaffected, while, in the case of merging jets, after the collision, the faster jet absorbs the slower jet, although not instantly (2nd column).

We quantify the effect of jet collisions by projecting the total energy density of the system to the (x, y) plane, e_z , and measuring the spread of e_z along a line parallel to the x axis (i.e. along a vertical line in Figure 3) at a distance of 15 kpc from the collision point ($e_z[15, y]$), and identify the two regimes of the parameter space resulting in bouncing and merging jets. In Figure 6 we plot the width of the projected total energy density where it is $\geq 5\%$ of its maximum value ($e_z[15, y] \geq 0.05 \times \text{Max}\{e_z[15, y]\}$) in a grid of impact parameter ($0 \leq P \leq 0.8$) and the velocity of the second jet (expressed as the Mach number, $4.4 \leq M_{\text{jet}} \leq 7.9$). The black-blue-green-orange-red colors represent increasing spread of the jet. When the jets merge the spread is limited because the second jet disappears (black and dark blue color pixels).

A trend can be seen clearly in Figure 6: the spread increases as the impact parameter and the velocity of the second jet increases. The jets merge when the impact parameter and the velocity of the second jet are small (magenta and dark blue pixels; P000V10, P000V12, P000V14, P015V10, P015V12, and P030V10, see Table 1), otherwise they bounce. Since the x components of the velocities of the jets have opposite signs, the relative value of this component decreases (it should be zero for $v_1 = v_2$), and, as a consequence, the angle between the bouncing jets decreases as does the spread between them. This is the reason for the increasing spread with increasing impact parameter (left to right in Figure 6). Even though both jets propagate in the positive y direction, the y component of the velocities of both jets decreases because, as they collide, they generate more turbulence and drive more waves as they propagate due to the increased instabilities.

3.2. Instabilities in Colliding Jets

In general, as the jets propagate in the ambient medium, instabilities are generated due to the Kelvin-Helmholtz process (e.g., Birkinshaw 1991; Ferrari 1998, and references therein). The form of the instabilities depends on the thickness of the contact layer between the jet and the ambient medium. Near the origin of the jet the transition zone is thin, and the vortex sheet approximation can be used assuming large density and velocity gradients. Farther from the origin, the contact layer extends due to matter entrainment, turbulence and other non-linear effects.

There are two main types of instability in jets: the surface modes, which have steeply decreasing amplitude as a function of the distance from the jet surface, and reflected body modes, which affect the entire gas in the jet. Reflection modes dominate if $M_{\text{jet}} \gtrsim 2\sqrt{2}$ (e.g., Ferrari 1998). The jet Mach numbers in our hydrodynamical simulations range from 4.4 to 7.9, therefore we expect the reflection modes to dominate. The wavelengths of the reflection modes can be estimated as $\lambda \sim 2\pi R M_{\text{jet}}$, where R is the characteristic cross section of the jet. In our case, $\lambda \sim 17 \text{ kpc}$. Our simulations show long wavelength oscillations along the jets with wavelengths in the range of 10 - 20 kpc, which is compatible to the expected wavelength of the reflection modes.

In the 3rd column in Figure 5 we show the total energy projected to the (x, y) plane from our colliding jet simulations with fixed jet velocities: $v_1 = v_2 = 18000 \text{ km s}^{-1}$, but different impact parameters: $P = 0.5, 1, 1.3$, and with $P = \infty$ representing two non-interacting pairs of jets (top to bottom; models: P045V18, P100V18, P130V18, and SNGV18). In the case of non-interacting jets (see bottom panel in the 3rd column), linear instabilities grow non-linear only after the jets travel about 20 kpc. However, it can be seen from the 3rd column in Figure 5 that the instabilities are enhanced in colliding jets and they grow non-linear soon or immediately after the collision (see 1st, 2nd and 3rd panels). As we increase the impact parameter, the instabilities decrease (top to bottom in the 3rd column; see also the trend from left to right in the different columns in Figure 3).

The jets in Figure 5 do not seem to expand where they meet, therefore the jets in our simulations with $P = 1$

and 1.3 do not actually collide. However, interestingly, comparing the 2nd and 3rd panels ($P = 1$ and 1.3) in Figure 5 with the last panel ($P = \infty$), we notice that the two jets still interact with each other via turbulence, which enhances the instabilities and generates oscillations traveling down the jets.

Studying the images from our hydrodynamic simulations, we notice that in some cases the jets break into filaments due to instabilities (e.g., models P080V18, P100V18, and SNGV18, columns 4, 5, and 6 top panels, and models P100V10, and SNGV10, columns 5 and 6 bottom panels in Figure 3). Our simulations show that, in general, filaments form in jets only far from the source (~ 30 kpc) unless the collision is strong, i.e., the impact parameter is small (e.g., models P045V18 and P080V18; compare top panels in columns 4 and 6). However, filaments of this form are not frequently seen in radio images of extragalactic jets, which is most likely due to the fact that the jets usually reach lower-pressure regions in the ambient medium and expand substantially before filaments could develop.

3.3. Enstrophy Generation in Colliding Jets

The effect of interaction between jets due to turbulence generated by collision can be quantified using the enstrophy density, the mean squared vorticity,

$$\Omega(\mathbf{r}) = \frac{1}{2} |\boldsymbol{\omega}(\mathbf{r})|^2, \quad (5)$$

where $\boldsymbol{\omega}(\mathbf{r}) = \nabla \times \mathbf{v}(\mathbf{r})$ is the vorticity at position \mathbf{r} (note that, occasionally, it is defined without the $1/2$ factor). In Figure 7 we show the integrated enstrophy (over x and z) as a function of distance from the jet source (the y coordinate) for different impact parameters: $P = 0, 0.15, 0.30, 0.45, 0.60, 0.80, 1.00, 1.3$, and ∞ in units of the jet diameter. The maximum distance to which the enstrophy shows the jets to propagate as coherent structures increases monotonically as the impact parameter is increased, while the enstrophy peak drops significantly at $P > 0.5$, as the jet centers become separated by more than one jet radius.

As the jets propagate, most of the enstrophy (turbulence) is generated near the jet (3rd panel in the first and second columns in Figure 5). In the top panel in Figure 7 we show the projected enstrophy, normalized to its value at injection for each model, as a function of the distance along the jet for $y \geq 0$ from the simulations of colliding jets with fixed jet velocities, $v_1 = v_2 = 18000 \text{ km s}^{-1}$, but with different impact parameters: $0 \leq P \leq \infty$ (see last row in Table 1, and P130V18). It can be seen from this figure that more enstrophy is generated right after the collision when we adopt smaller impact parameters. The largest enstrophy peaks (> 6) belong to the four smallest impact parameters ($P = 0, 0.15, 0.30, 0.45$).

The bottom panel of Figure 7 shows the maximum of the enstrophy as a function of the impact parameter for interacting jets ($0 \leq P \leq 1.3$). The enstrophy maximum shows a “phase transition” as a function of the impact parameter at a critical point, $P_{\text{crit}} \sim 0.5$. Small impact parameters, $0 \leq P \lesssim P_{\text{crit}}$, result in large enstrophy maxima, ~ 9 , in the transition region around P_{crit} , the enstrophy drops to about half of this value, and for large impact parameters, $P_{\text{crit}} \lesssim P \leq 1.3$, the maximum is ~ 4.6 . A likely explanation for this “phase

transition” is the following. At the collision region of the two jets, the jets slightly oscillate in direction as a result of the growing Kelvin-Helmholtz instabilities. These oscillations induce a change in the jet gas mass involved directly in the collision by changing the collision cross section. The larger the changes in the mass involved in the collision, the more turbulence is generated driving more shock waves into the ambient medium resulting larger enstrophy maxima. The change in the mass involved in the collision is larger for small impact parameters, generating more turbulence. As we increase the impact parameter, the change in the jet gas mass due to the oscillations of the jets drops at around $P \sim 0.5$, and, as a consequence, the amount of turbulence and thus the enstrophy maximum are also reduced significantly.

As the jets are plunging through the ambient gas, their bulk kinetic energy dissipates into shocks and turbulence, and, as a result, they slow down. The dissipation of the bulk kinetic energy into turbulent energy can be quantified using the enstrophy density. The scalar product of the curl of Equation 2 with $\boldsymbol{\omega}$ leads to the equation for enstrophy generation along the jet,

$$\frac{D\Omega}{Dt} = \boldsymbol{\omega} \cdot (\boldsymbol{\omega} \cdot \nabla) \mathbf{v} - 2\Omega(\nabla \cdot \mathbf{v}) + \boldsymbol{\omega} \cdot (\nabla \rho \times \nabla p) / \rho^2, \quad (6)$$

where the left hand side of this equation is the Lagrangian derivative, $D\Omega/Dt = \partial\Omega/\partial t + (\mathbf{v} \cdot \nabla)\Omega$, and the source terms on the right hand side are the enstrophy stretching term, the compression term, and the baroclinic contribution, which is a result of the misalignment between the gradients of the gas density and the pressure (e.g., Porter et al. 2015).

We illustrate the generation of enstrophy using our simulation with a small impact parameter, $P = 0.15$, and injection velocities $v_1 = v_2 = 18000 \text{ km s}^{-1}$. In Figure 8 we show the relative contributions from the 1st, 2nd, and 3rd terms in Equation 6 to the enstrophy generation (blue, green and red lines). Note that these terms represent enstrophy generation rates and therefore their dimension is enstrophy over time. For comparison, we also show the enstrophy (black solid line) normalized to its value at the injection (also shown in Figure 7). It can be seen clearly from this figure that the compression and the baroclinic terms (2nd and 3rd terms in Equation 6) are fluctuating around zero, thus their time integral will be negligible and they do not contribute significantly to the enstrophy. The stretching term (1st term in Equation 6) has a shape similar to the of the enstrophy (black solid line). As expected, this term is always positive (e.g., Buxton & Ganapathisubramani 2010), and, as a consequence, the contribution from stretching dominates the enstrophy generation. Note, however, that Buxton & Ganapathisubramani (2010) used equations of incompressible fluid dynamics in their analysis, and our simulations were based on compressible fluid dynamics, which is more appropriate for astrophysical applications.

3.4. Applications to 3C 75

The two bipolar jet system in 3C 75 is located in the dumbbell shaped twin Wide Angle Tail (WAT) radio galaxy NGC 1128 at the center of the nearby galaxy cluster Abell 400 at a redshift of 0.023 (e.g., Owen et al. 1985; Hudson et al. 2006). Hudson et al. (2006) concluded that the AGNs in 3C 75 form a bound system originating from

a previous merger, and they are both contained in a low entropy core moving through the intracluster medium at a relative speed of 1200 km/sec. In Figure 1 the radio and optical (SDSS) images of 3C 75 are shown with green and red colors (Hardcastle & Sakelliou 2004). The two AGNs, the sources of the jets, at the center of the image, are located at about 7 kpc from each other in projection.

3C 75 is one of the best sources to study the different physical mechanisms capable of bending jets (e.g., ram pressure due to the ambient gas as the jets move, collision with dense gas in the ambient medium, and collision with other jets). The ram pressure from a medium in transverse relative motion to the jet is the most common reason why jets show large-scale bends. The smooth changes in the direction of the jets in 3C 75 farther from their AGNs are due to the relative movement of the AGNs to the ambient medium. The direction of the bending of the jets (towards north-east) suggests that 3C 75 is moving to the south-west. The eastern jet of the northern AGN seems to bend suddenly to the north about 25 kpc east of the core, where an enhancement can be seen in the X-ray emission (Hudson et al. 2006), perhaps because of an encounter with a denser gas cloud in the intergalactic medium, or with the atmosphere of a galaxy. However, the western jet from the northern AGN, after traveling about 15 kpc from its source, bends to the north by about 45° where its path crosses that of the northern jet of the southern AGN. No X-ray enhancement associated with extra gas can be seen in this location and the southern AGN seems to be propagating towards the north-west without changing its direction (Hudson et al. 2006). This morphology suggests that the bending of the jet from the northern AGN at this location is a result of a collision with the jet from the southern AGN.

In Figure 9 we show projections of the total energy and helicity along the jet in the interaction region (left and right panels) from our simulation with $v_1 = 18000$ km s $^{-1}$ and $v_2 = 10000$ km s $^{-1}$, and an impact parameter of $P = 0.3$ (model P030V10) using different rotation angles around the direction of the propagation of the jet: $\varphi = 0^\circ, 30^\circ, 60^\circ, 90^\circ, 120^\circ, 150^\circ$ (top to bottom). Blue, red, and white colors represent positive, negative, and zero helicities. In projection, a double helical feature can be seen in some viewing angles (especially at $\varphi = 0^\circ$), which may give the impression that the two jets are spiraling around each other. However, our simulation shows that, in this case the jets merge, the faster jet takes over the slower one, and breaks into filaments due to the enhanced instabilities arising from the collision. The two filaments travel with a speed close to that of the faster jet and have no coherent rotational velocities perpendicular to their propagation, which would be necessary for helical motion. However, the filaments seem to have different helicities, coherent on the scale of a few kpc along their propagation direction, which may provide stability to these oscillating filaments (right column in Figure 9).

Our hydrodynamical simulations suggest a possible physical explanation for the morphology of 3C 75. The slower northern jet from the northern AGN collides with a small but finite impact parameter with the faster jet from the southern AGN traveling towards north-west, the jets merge, and the faster jet takes over the slower jet (most of the gas from the slower jet is grabbed by

the faster jet). The helical-looking morphology is a projection effect: the faster jet breaks into filaments due to the enhanced instabilities caused by the collision with the slower jet. This explanation is consistent with all observed features of 3C 75.

4. CONCLUSION

We carried out hydrodynamical simulations to study extragalactic jet collisions. We found that colliding jets can be cast into two categories: bouncing and merging jets. We have shown that two fast jets colliding with non-zero impact parameter bounce off each other keeping their identities, but jets with very different velocities colliding with a small impact parameter merge into one jet, and the faster jet takes over the slower jet. We have found that the collision enhances the instabilities of the jets; kpc scale oscillations are generated, and the jets may break up into filaments. In some projections, the filaments may show a twisted structure.

In general, magnetic fields in jets can reduce the growth of the Kelvin-Helmholtz instabilities, and, as a consequence, generate less turbulence, and can also affect the transport processes within the jets (e.g., Hardee 2004; Ferrari 1998). However, the collisions between fast jets included in our simulations are so energetic that we expect that the weak magnetic fields inferred from observations would affect neither the dynamics of the collisions significantly, nor our qualitative results on bouncing and merging of jets.

Our hydrodynamical simulations suggest a physical explanation for the twisted radio morphology of 3C 75: strong instabilities are generated in the faster jet by the collision with a much slower jet with a small, but finite impact parameter. We leave a more quantitative analysis of 3C 75 for a future study.

We thank the anonymous referee for detailed comments and suggestions, which helped to improve the presentation of our results. The code *FLASH* used in this work was in part developed by the DOE-supported ASC/Alliance Center for Astrophysical Thermonuclear Flashes at the University of Chicago. This research has made use of the NASA/IPAC Extragalactic Database (NED) which is operated by the Jet Propulsion Laboratory, California Institute of Technology, under contract with the National Aeronautics and Space Administration.

TABLE 1
IDS AND THE GRID OF INPUT PARAMETERS FOR DIFFERENT MODELS USED IN OUR HYDRODYNAMICAL SIMULATIONS.

v_1^a	v_2^b	M_{jet}^c	$P = 0^d$	$P = 0.15^d$	$P = 0.30^d$	$P = 0.45^d$	$P = 0.60^d$	$P = 0.80^d$	$P = 1^d$	$P = \infty^e$
18	18	7.9	P000V18	P015V18	P030V18	P045V18	P060V18	P080V18	P100V18	SNGV18
18	16	7.0	P000V16	P015V16	P030V16	P045V16	P060V16	P080V16	P100V16	SNGV16
18	14	6.1	P000V14	P015V14	P030V14	P045V14	P060V14	P080V14	P100V14	SNGV14
18	12	5.3	P000V12	P015V12	P030V12	P045V12	P060V12	P080V12	P100V12	SNGV12
-	10	4.4	P000V10	P015V10	P030V10	P045V10	P060V10	P080V10	P100V10	SNGV10

NOTE. — The IDs indicate the impact parameters and velocities of the second jet.

^a Injection velocity of the 1st jet in 1000 km s⁻¹ (fixed).

^b Injection velocity of the 2nd jet in 1000 km s⁻¹.

^c Jet Mach number of the 2nd jet.

^d Impact parameters, P , in units of the jet radius (see Section 2.1).

^e Impact parameter of $P = \infty$ refers to our single jet models with different injection velocities (v_2).

REFERENCES

- Birkinshaw, M. 1991, MNRAS, 252, 505
 Buxton, O., R., H. & Ganapathisubramani, B., 2010, J. Fluid Mech., 651, 483
 Colella, P. 1990, J. Comput. Phys., 87, 171
 Colella, P., & Woodward, P. R. 1984, J. Comput. Phys., 54, 174
 Edge, A. C. 2001, MNRAS, 328, 762
 Fabian A. C., 1994, ARA&A, 32, 277
 Fabian, A. C. 2012, ARA&A, 50, 455
 Falceta-Gonçalves, D., de Gouveia Dal Pino, E. M., Gallagher, J. S., & Lazarian, A. 2010, ApJ, 708, L57
 Feretti, L., Perley, R., Giovannini, G., & Andernach, H. 1999, A&A, 341, 29
 Ferrari, A. 1998, ARA&A, 36, 539
 Fryxell, B., Olson, K., Ricker, P., et al., 2000, ApJS, 131, 273
 Gaspari, M., Melioli, C., Brighenti, F., & D’Ercole, A. 2011, MNRAS, 411, 349
 Gaspari, M., Ruszkowski, M., & Oh, S. P. 2013, MNRAS, 432, 3401
 Gaspari, M., Ruszkowski, M., & Sharma, P. 2012, ApJ, 746, 94
 Hardcastle, M. J., & Sakelliou, I. 2004, MNRAS, 349, 560
 Hardee, P. E. 2004, Ap&SS, 293, 117
 Hudson, D. S., Reiprich, T. H. Clarke, T. E. & Sarazin, C. L. 2006, A&A 453, 433
 Laing, R. A., & Bridle, A. H. 2014, MNRAS, 437, 3405
 Laing, R. A., Parma, P., de Ruiter, H. R., & Fanti, R. 1999, MNRAS, 306, 513
 Li, Y., & Bryan, G. L. 2014a, ApJ, 789, 54
 Li, Y., & Bryan, G. L. 2014b, ApJ, 789, 153
 Li, Y., Bryan, G. L., Ruszkowski, M., et al. 2015, ApJ, 811, 73
 Martizzi, D., Teyssier, R., & Moore, B. 2012, MNRAS, 420, 2859
 McDonald, M., Veilleux, S., & Mushotzky, R. 2011, ApJ, 731, 33
 McNamara, B. R., & Nulsen, P. E. J. 2007, ARA&A, 45, 117
 Mignone, A., & McKinney, J. C. 2007, MNRAS, 378, 1118
 O’Dea, C. P., Baum, S. A., Privon, G., et al. 2008, ApJ, 681, 1035
 Owen, F. N., O’Dea, C. P., Inoue, M., & Eilek, J. A. 1985, ApJ, 294, L85
 Peterson, J. R., Kahn, S. M., Paerels, F. B. S., et al. 2003, ApJ, 590, 207
 Peterson, J. R., & Fabian, A. C. 2006, Phys. Rep., 427, 1
 Pizzolato, F., & Soker, N. 2005, ApJ, 632, 821
 Porter, D. H., Jones, T. W., & Ryu, D. 2015, ApJ, 810, 93
 Pudritz, R. E., Hardcastle, M. J., & Gabuzda, D. C. 2012, Space Sci. Rev., 169, 27
 Roe, P. L. 1981, J. Comput. Phys., 43, 357
 Salomé, P., & Combes, F. 2003, A&A, 412, 657
 Schive, H.-Y., Zhang, U.-H., & Chiueh, T. 2012, IJHPCA, 26, 367
 Schive, H.-Y., Tsai, Y.-C., & Chiueh, T. 2010, ApJS, 186, 457
 Tamura T., Kaastra J. S., Makishima K., & Takahashi I., 2003, A&A, 399, 497
 Trac, H., & Pen, U.-L. 2003, PASP, 115, 303
 Van Loo, S., Tan, J. C., & Falle, S. A. E. G. 2015, ApJ, 800, L11
 Yang, H.-Y. K., & Reynolds, C. S. 2016, ApJ, 818, 181

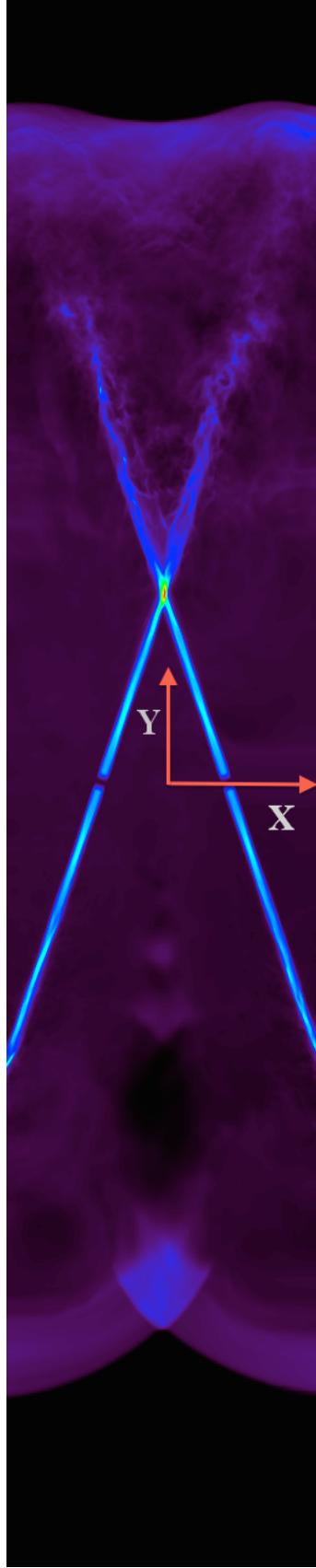


FIG. 2.— Total energy density of our colliding jet model with velocities of $v_1 = v_2 = 18000 \text{ km s}^{-1}$ and an impact parameter of $P = 0.6$ in units of the jet radius (see Section 2.1; model P060V18) projected to the (x, y) plane. The simulation box size is $(x, y, z) = (\pm 10, \pm 50, \pm 10)$ kpc.

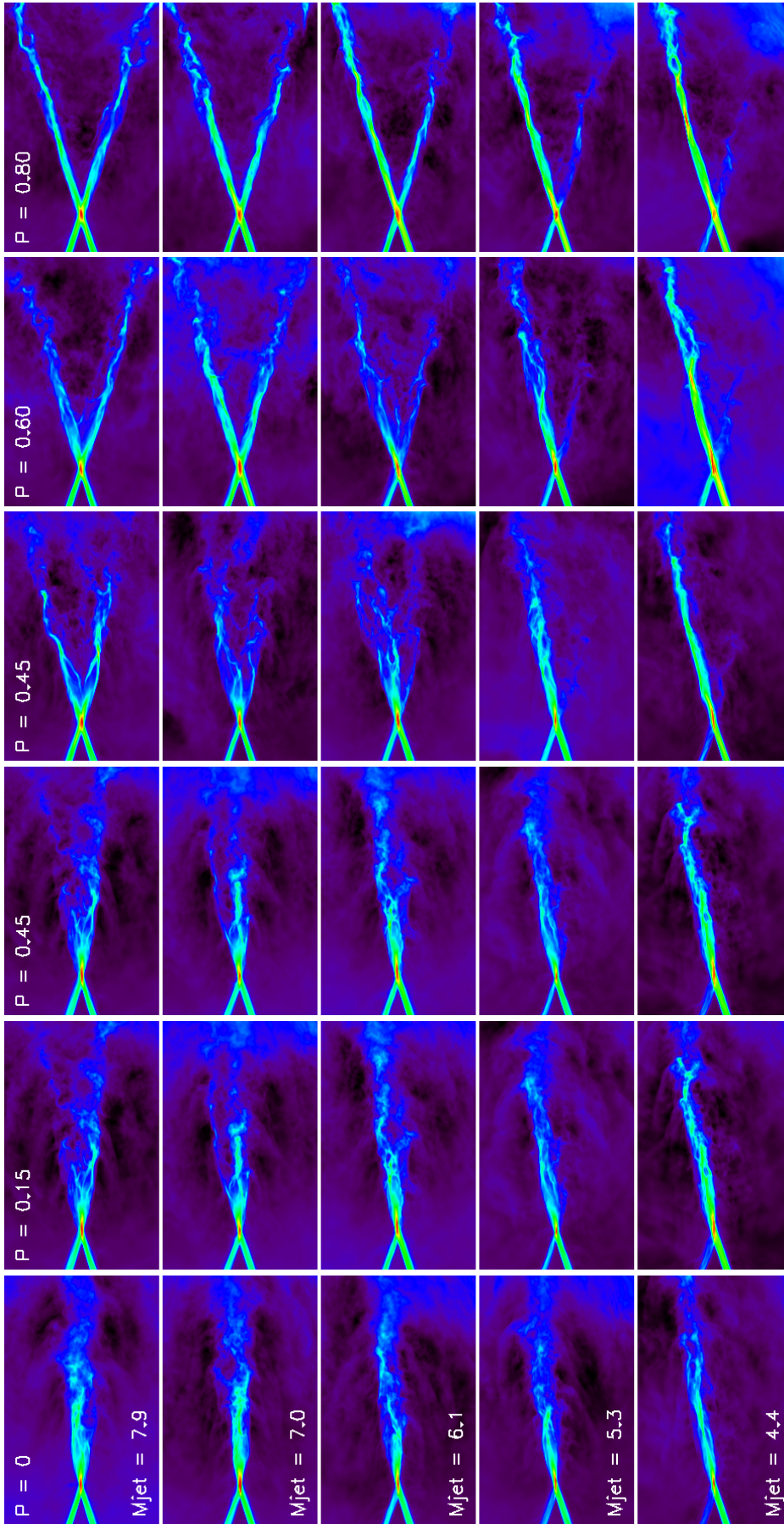


FIG. 3.— Total energy density (log scale) of colliding jets from our simulations projected to the (x, y) plane with different impact parameters and injection velocities of the second jet. Columns relate to distinct impact parameters, P (in units of the diameter of the jet) given at the top of each column, and rows relate to distinct values of the jet internal Mach number, M_{jet} . The faster jet is propagating from the lower right to the upper left with a fixed Mach number of 7.9. See Section 2.1 for the details of the initial set up of our simulations. The red region located on the left hand side of each panel marks enhanced total energy due to the collision of the two jets.

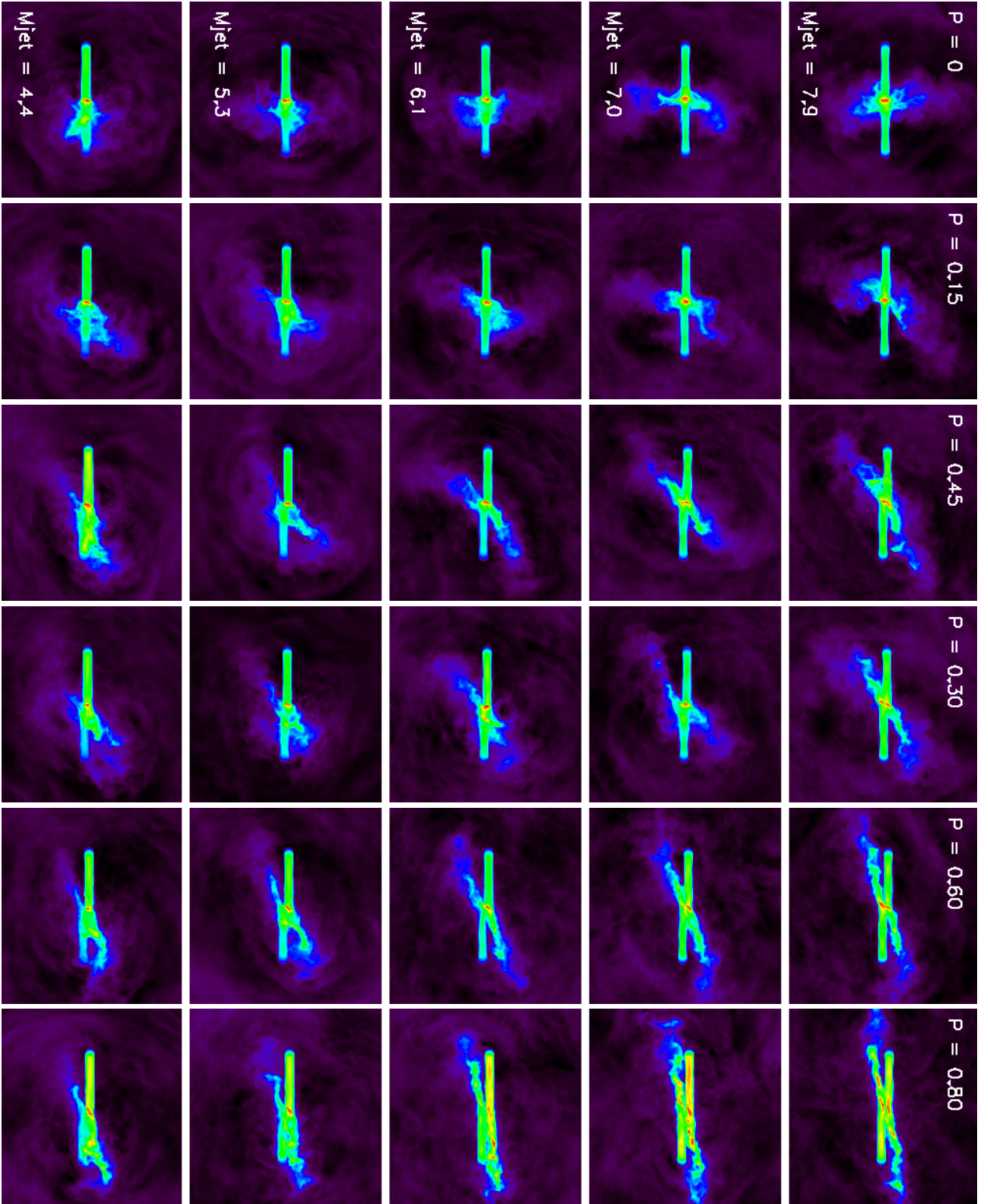


FIG. 4.— Same as Figure 3, but in projection to the (x, z) plane. The faster jet moves from left to right along the x axis with a fixed injection velocity, the second jet moves from right to left with different velocities. The collision region in the middle of each panel is marked with red.

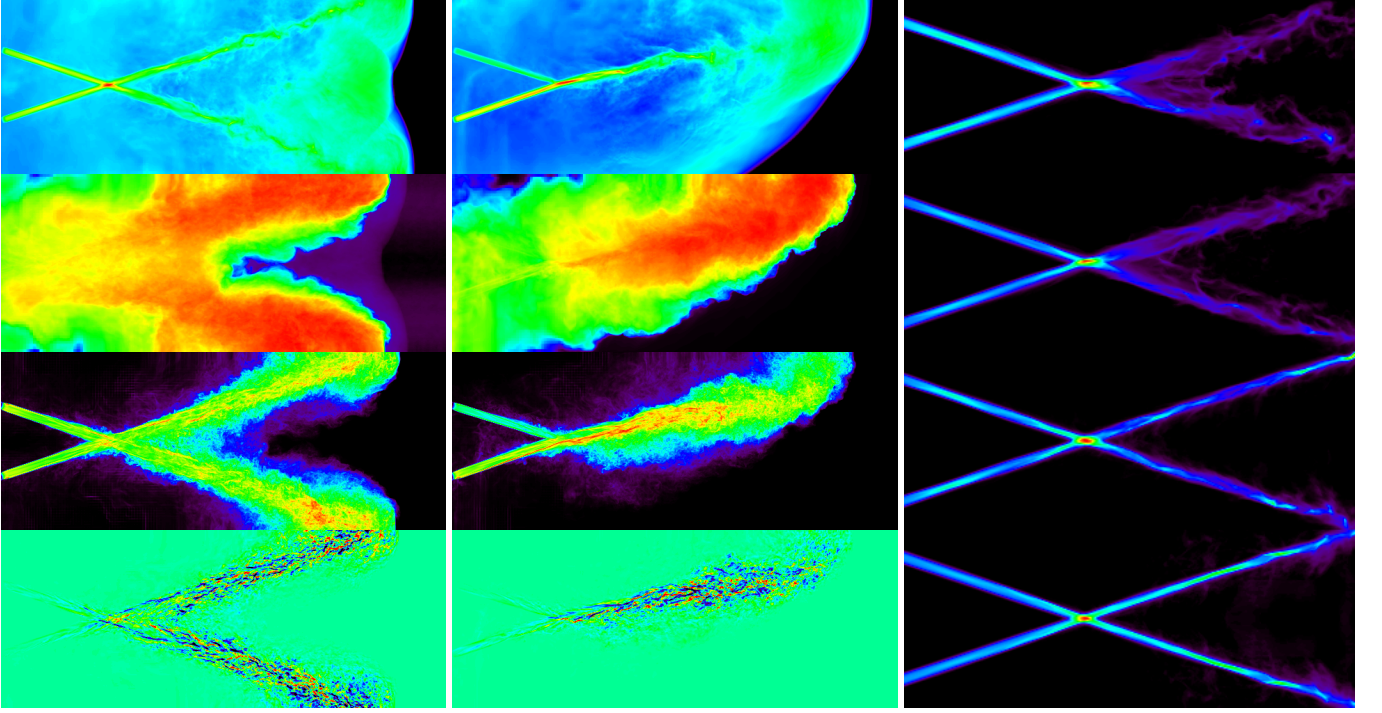


FIG. 5.— Physical parameters of bouncing and merging jets projected to the (x, y) plane. The jets propagate from left to right. The 1st column shows the total energy density, scaled entropy per particle, enstrophy (all in log scale), and helicity (linear scale) from our bouncing of jet simulation with $v_1 = v_2 = 18000 \text{ km s}^{-1}$, and a large impact parameter, $P = 0.8$. The 2nd column displays projections of the same physical quantities from our merging jet simulation with a small impact parameter, $P = 0.3$, and large velocity difference: $v_1 = 18000 \text{ km s}^{-1}$, $v_2 = 10000 \text{ km s}^{-1}$. Panels in the 3rd column show the total energy projected to the (x, y) plane from our bouncing jet simulations with fixed jet velocities of $v_1 = v_2 = 18000 \text{ km s}^{-1}$, but different impact parameters: $P = 0.5, 1.0, 1.3$, and ∞ in units of the jet diameter (see Section 2.1).

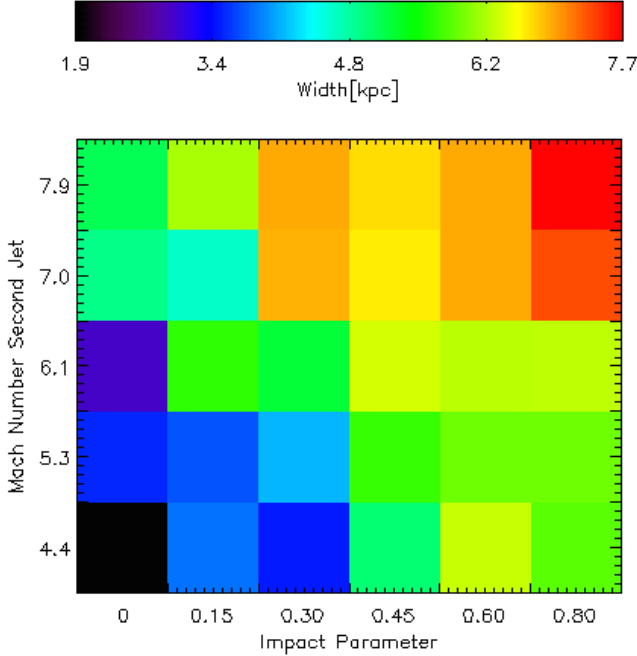


FIG. 6.— The spread around the maximum value of the total energy of colliding jets projected to the (x, y) plane, $e_z(x, y)$. The color scale represents the width of e_z where $e_z \geq 5\%$ of its maximum value at a distance of 15 kpc from the collision point ($e_z[15, y] \geq 0.05 \times \text{Max}\{e_z[15, y]\}$; see Section 3.1) as a function of impact parameter ($P = 0, 0.15, 0.3, 0.45, 0.6$ and 0.8 in units of the diameter of the jet) and the Mach number of the second jet ($M_{\text{jet}} = 4.4, 5.3, 6.1, 7.0$, and 7.9).

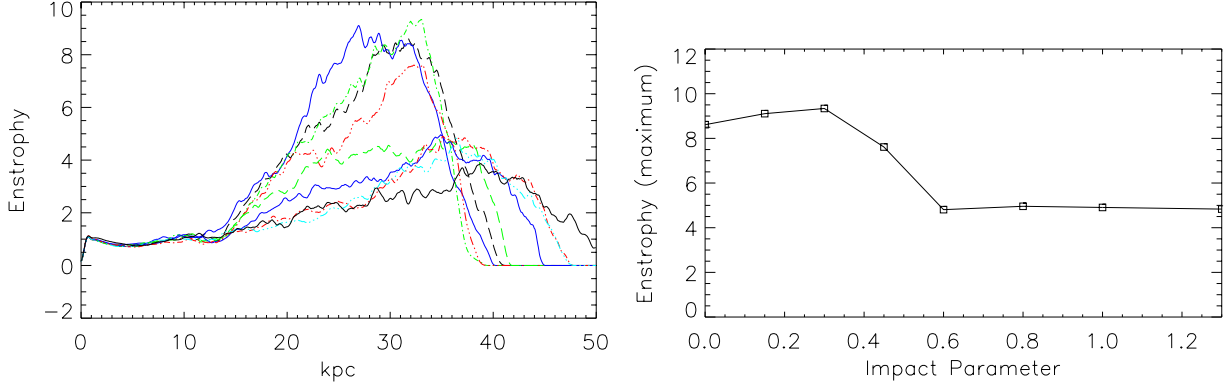


FIG. 7.— Top Panel: Projected enstrophy as a function of distance along the jet from our hydrodynamical simulations of colliding jets with different impact parameters: $P = 0, 0.15, 0.30, 0.45$ (black/dashed, blue/solid, green/dash-dotted, red/dash-dot-dot-dotted lines) with enstrophy maximum greater than 6, and $P = 0.60, 0.80, 1.00$, and 1.3 (green/dashed, blue/solid, red/dash-dot-dot-dotted, and aqua/dash-dotted lines) with maximum less than 6 in units of the diameter of the jet with fixed injection velocities: $v_1 = v_2 = 18000 \text{ km s}^{-1}$. The black/solid line extending farther than 50 kpc represents non-interacting jets ($P = \infty$). The enstrophy is normalized to its value at injection for each model. Bottom Panel: The maximum values of the enstrophy as a function of the impact parameter (from data displayed in the top panel).

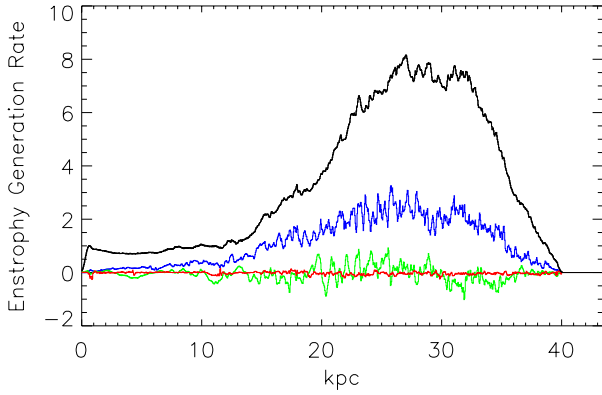


FIG. 8.— Enstrophy generation rate as a function of distance along the jet from our hydrodynamical simulations of colliding jets with impact parameter $P = 0.15$ and injection velocities $v_1 = v_2 = 18000 \text{ km s}^{-1}$. The blue, green and red lines represent the relative contributions to the enstrophy generation from stretching, compression, and from the baroclinic term (the 1st 2nd and 3rd terms in Equation 6). For comparison, we also show the enstrophy (black solid line) normalized to its value at the injection (also shown in Figure 7).

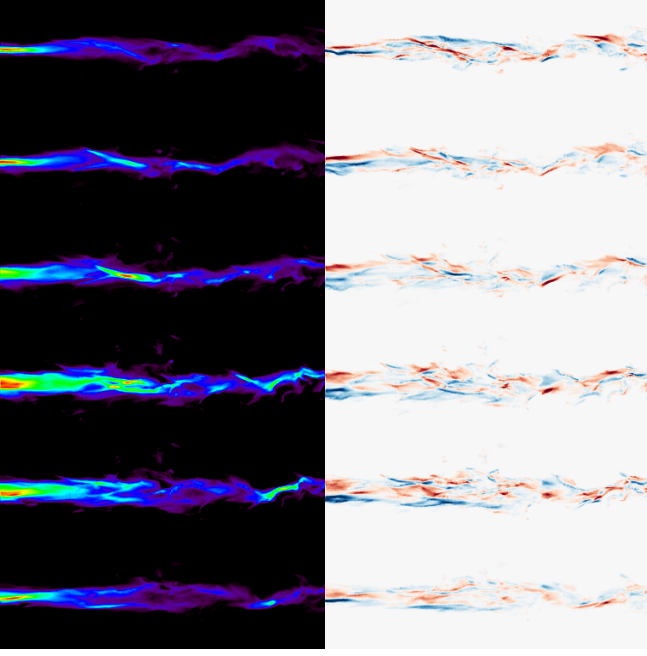


FIG. 9.— Projections of the total energy and helicity (left and right panels) of the two jets just after the collision using different rotation angles around the direction of the jet velocity (left to right): $\varphi = 0^\circ, 30^\circ, 60^\circ, 90^\circ, 120^\circ, 150^\circ$ (top to bottom) from our hydrodynamical simulations with jet injection velocities of $v_1 = 18000 \text{ km s}^{-1}$ and $v_2 = 10000 \text{ km s}^{-1}$, and an impact parameter of $P = 0.3$. Blue and red colors represent positive and negative helicities.